# Three-dimensional structure of the basketweave Z-band in midshipman fish sonic muscle

Thomas Burgoyne[a,1,2], John M. Heumann[b,1], Edward P. Morris[c,1], Carlo Knupp[d,1], Jun Liu[e,3], Michael K. Reedy[f,4], Kenneth A. Taylor[e], Kuan Wang[g,h], and Pradeep K. Luther[a,5]

[a]Molecular Medicine Section, National Heart and Lung Institute, Imperial College London, SW7 2AZ London, United Kingdom; [b]Department of Molecular, Cellular and Developmental Biology, University of Colorado, Boulder, CO 80309-0347; [c]Division of Structural Biology, Institute of Cancer Research, SW7 3RP London, United Kingdom; [d]School of Optometry and Vision Sciences, Cardiff University, CF10 3AT Cardiff, United Kingdom; [e]Institute of Molecular Biophysics, Florida State University, Tallahassee, FL 32306-4380; [f]Department of Cell Biology, Duke University Medical Center, Durham, NC 27710; [g]Laboratory of Muscle Biology, National Institute of Arthritis and Musculoskeletal and Skin Diseases, NIH, Bethesda, MD 20892; and [h]College of Biomedical Engineering, Taipei Medical University, Taipei 11031, Taiwan

Edited by James A. Spudich, Stanford University School of Medicine, Stanford, CA, and approved June 24, 2019 (received for review February 7, 2019)

**Striated muscle enables movement in all animals by the contraction of myriads of sarcomeres joined end to end by the Z-bands. The contraction is due to tension generated in each sarcomere between overlapping arrays of actin and myosin filaments. At the Z-band, actin filaments from adjoining sarcomeres overlap and are cross-linked in a regular pattern mainly by the protein α-actinin. The Z-band is dynamic, reflected by the 2 regular patterns seen in transverse section electron micrographs; the so-called small-square and basketweave forms. Although these forms are attributed, respectively, to relaxed and actively contracting muscles, the basketweave form occurs in certain relaxed muscles as in the muscle studied here. We used electron tomography and subtomogram averaging to derive the 3D structure of the Z-band in the swimbladder sonic muscle of type I male plainfin midshipman fish (*Porichthys notatus*), into which we docked the crystallographic structures of actin and α-actinin. The α-actinin links run diagonally between connected pairs of antiparallel actin filaments and are oriented at an angle of about 25° away from the actin filament axes. The slightly curved and flattened structure of the α-actinin rod has a distinct fit into the map. The Z-band model provides a detailed understanding of the role of α-actinin in transmitting tension between actin filaments in adjoining sarcomeres.**

Z-line | Z-disc | α-actinin | electron tomography | subtomogram averaging

Striated muscles are agglomerates of myriads of sarcomeres joined end to end by the Z-bands (Z-lines, Z-discs) and contraction of muscle occurs when sarcomeres shorten. Each sarcomere comprises 2 inwardly facing arrays of actin filaments which are attached at the Z-band at one end and overlap at the other end with the centrally located array of myosin filaments (1). Sarcomere shortening is due to the actin filaments moving past the myosin filaments toward the center of the sarcomere. The barbed ends of actin filaments of adjoining sarcomeres overlap in the Z-band and are cross-linked in precise patterns mainly by the rod-shaped protein α-actinin.

The Z-band in vertebrate striated muscle is dynamic and in cross-sectional view manifests 2 patterns, the so-called basketweave and small-square lattice forms (1–3). In this study we examine the structure of the basketweave Z-band of a specialized muscle, the midshipman fish sonic muscle, in the relaxed state. However, the 2 forms are generally thought to result from the contractile state of the muscle, the basketweave attributed to contracting muscle while the small-square form is attributed to relaxed muscle. As there is a physical change in the Z-band during contraction, it may have a role in mechanotransduction. It is thought that the small-square form is due to sharply bent Z-band links, whereas the basketweave form is due to straightening of the links and a small lattice expansion as could occur during contraction (2, 3). However, the molecular nature of this transformation is not known. We note that the basketweave form in relaxed muscle has been seen in other species: fish fin muscle (4) and bovine neck muscle (5). It is not known what form the Z-bands of these muscles adopt during contraction. Some researchers have proposed that the Z-band state may be due to the state of tropomyosin on actin (2).

In longitudinal view, the Z-band presents as a dense band defining sarcomere boundaries. The Z-band has a characteristic width which depends on the muscle type: it is narrowest in fast muscles (~60 to 100 nm) and wider in slow and cardiac muscles (100 to 140 nm) (6). The Z-band is the location of a multitude of proteins with various functions, and mutations in these proteins lead to skeletal and cardiac disease (7).

The variation in Z-band width between different muscle types noted above arises from the extent of overlap between the actin filaments from adjacent sarcomeres and the number of layers of the zig-zag structure arising from the connecting links between actin filaments (6). The primary component of these connecting links in the Z-band is α-actinin, a member of the spectrin family. α-Actinin is a ubiquitous protein in the eukaryote cytoskeleton (8–10); it is a homodimer of length 360 Å whose crystal structure was solved recently (11). It is composed of 2 antiparallel rod-shaped

## Significance

Striated muscle enables movement in all animals by the contraction of myriads of sarcomeres joined end to end by the Z-bands. The contraction is due to tension generated in each sarcomere between overlapping arrays of actin and myosin filaments. At the Z-band, actin filaments from adjoining sarcomeres overlap and are cross-linked mainly by the protein α-actinin. In this study, we used electron tomography and subtomogram averaging to derive the 3-dimensional structure of the Z-band in swimbladder muscle of plainfin midshipman fish, into which we docked the atomic coordinates of actin and α-actinin. The Z-band model provides a detailed understanding of the role of α-actinin in transmitting tension between actin filaments in adjoining sarcomeres.

Author contributions: M.K.R., K.W., and P.K.L. designed research; T.B., C.K., J.L., and P.K.L. performed research; M.K.R., K.A.T., and K.W. contributed new reagents/analytic tools; T.B., J.M.H., E.P.M., and P.K.L. analyzed data; and E.P.M. and P.K.L. wrote the paper.

The authors declare no conflict of interest.

This article is a PNAS Direct Submission.



Data deposition: The sonic muscle Z-band map has been deposited to the Electron Microscopy Data Bank, www.emdatabank.org (accession code EMD-10113).

[1]T.B., J.M.H., E.P.M., and C.K. contributed equally to this work.

[2]Present address: Institute of Ophthalmology, University College London, London, EC1V 9EL.

[3]Present address: Department of Microbial Pathogenesis, Yale School of Medicine, New Haven, CT 06510.

[4]Deceased 18 June 2019.

[5]To whom correspondence may be addressed. Email: p.luther@imperial.ac.uk.

This article contains supporting information online at www.pnas.org/lookup/suppl/doi:10.1073/pnas.1902235116/-/DCSupplemental.

Published online July 18, 2019.

monomers. Each monomer is composed of an N-terminal actin binding domain (ABD) consisting of 2 calponin homology domains (CH1 and CH2), a rod domain comprising 4 spectrin domains, and a C-terminal region comprising 2 pairs of EF hand domains, EF1-2 and EF3-4 (11). While the ABD is flexible and can bind actin in a variety of conformations (12), the rod domain is rigid with a small curve (11, 13).

To understand the Z-band dynamic states exhibiting small-square and basketweave conformations, we need to determine the structures of these states at a resolution sufficient for docking the atomic models of actin and α-actinin. Ideally, the sample should be homogeneous in morphology. It is fortuitous that the structure of the sarcomere in all vertebrate striated muscle, including skeletal and cardiac, is very similar, which gives us the freedom to select the most favorable sample for a particular study (14). The muscle surrounding the swimbladder of type I male plainfin midshipman fish (*Porichthys notatus*) provides a favorable sample of the basketweave Z-band form. Whereas normal Z-bands have narrow axial widths ranging from 60 to 140 nm discussed above, this so-called sonic muscle has a highly specialized Z-band which is exceptionally wide at ∼1.2 μm (Fig. 1*A*) and highly ordered (Fig. 1 *B*–*D*): its unusual width arises from multiple layers of the underlying α-actinin linkage (15). The multiple layers contribute to the high level of order of the sonic Z-band as well as greatly increasing the number of individual repeating structures available for averaging. These factors make the sonic Z-band particularly favorable for structure determination by electron microscopy. Apart from the unusual width of the Z-band, the A-bands and sarcomeres of the sonic muscle are normal, although the myofibrils are significantly narrower than other muscle types (∼0.2 μm). *P. notatus* are normally deep sea fish which emerge into coastal regions during the mating season and make low-frequency (∼100 Hz) humming sounds with these sonic muscles (16).

In this study we have elucidated the 3D structure of the Z-band in the basketweave form in the sonic muscle of midshipman fish by electron tomography and subtomogram averaging. Our reconstruction has enabled us to fit the crystallographic structures of α-actinin and actin into the map, solving 1 of the 2 main conformational states of the vertebrate Z-band and giving a detailed understanding of the role of the Z-band in transmitting tension between actin filaments in adjoining sarcomeres.

## Results

For this study, we used ∼100-nm-thick transverse sections of resin-embedded sonic muscle Z-band. The muscle was treated in 50 mM butanedione-monoxime (BDM), an inhibitor of skeletal muscle myosin (17) thereby ensuring that the muscle is in a relaxed state. Electron microscopy of transverse sections showed a clear homogeneous basketweave form (Fig. 1*D* and *SI Appendix*, Fig. S1*A*). Although we collected tomograms of both transverse and longitudinal sections for this study, the former were found to

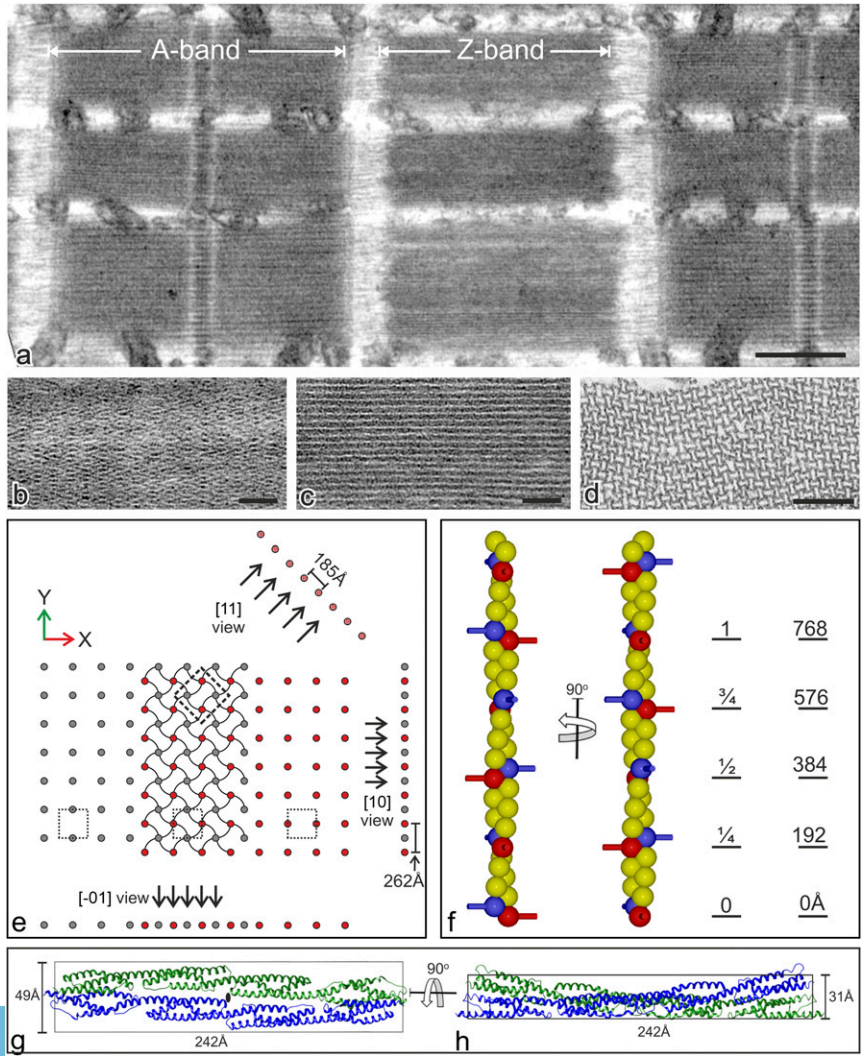


**Fig. 1.** The extraordinarily wide Z-band of midshipman fish and schematic drawings of relevant structures. (*A*–*D*) Electron micrographs of thin sections of swimbladder muscle of type I male plainfin midshipman fish. (*A*) Longitudinal section shows exceptionally wide (axially) ∼1.2-μm Z-bands with normal A-bands. (*B* and *C*) Longitudinal sections of the Z-band showing clear lattice views; (*B*) [10] view, and (*C*) [11] view. (*D*) Transverse section showing clear basketweave form. The lattice is ordered over ∼200-nm clusters with clear dislocations between them. (*E*) The Z-band tetragonal lattice and nomenclature of lattice views. The main figure illustrates a slightly oblique lattice of actin filaments of one sarcomere (gray) at the left and actin filaments from an adjoining sarcomere at the right (red) and interdigitation of the filaments in the basketweave Z-band. Along the bottom, unit cells are outlined in the Z-band and on either side. Projecting about the major axes gives the lattice views we observe in longitudinal sections, like the [10] view with spacing 262 Å and similar orthogonal [01] view. Projecting along the diagonal gives the [11] view with spacing 185 Å. The dashed line box shows the size used for subvolume averaging (discussed in *Results*). (*F*) An actin filament can be thought of as a 1-start, shallow helix in which the monomers are related by an axial rise of 27.4 Å and a rotation of 167.1° so that every seventh actin subunit is spaced 192 Å apart axially and rotated by 90° forming $4_3$ screw symmetry. Binding sites for α-actinin are highlighted in red and blue to emphasize the screw symmetry of the paired binding sites. (*G* and *H*) α-Actinin rod (13) fits into a rectangular slab of length 242 Å, width 49 Å (*G*), and depth 31 Å (*H*). The slab face (*G*) comprises the 2-fold view (marked with central symbol) and the slab edge (*H*) shows the gently curved structure of the rod. (Scale bars: 0.5 μm in *A*, 100 nm in *B*–*D*.)

be much more informative and are described here. The results of the latter are briefly described later. Tomograms were calculated from tilt series of sections of the sonic muscle Z-band as described in *Materials and Methods*. An image of the projected tomogram is shown in *SI Appendix*, Fig. S1*A*; it comprises 2 myofibrils in cross-section. A movie paging through the depth of the tomogram is shown in Movie S1. As the sonic muscle Z-band is a 3D crystal, the movie shows recurring basketweave motifs through the depth of the tomogram.

Scrutiny of the Z-band in Fig. 1*D* and *SI Appendix*, Fig. S1*A* shows that the Z-band is based on an approximate tetragonal lattice but the lattice is not coherent over the whole myofibril. The lattice is regular over small ∼200-nm clusters like the example outlined in *SI Appendix*, Fig. S1*A*. Viewing the image at a glancing angle accentuates the boundaries between the ordered clusters and shows up the dislocations between them. To obtain a mean 3D image of the Z-band, various methods can be used. As these clusters are quite small, crystallographic tilt reconstruction (18, 19) cannot be used. We decided to use subtomogram averaging using as our subvolume (or particle) the Z-band region as outlined with a dashed box in the *Upper* part of the Z-band in Fig. 1*E*.

To enable accurate subtomogram averaging and symmetrization over subvolumes with varying orientations, it is essential that the sample not be distorted. Thin sections of plastic-embedded samples as used in this study are typically compressed during ultramicrotomy. Our correction of the compression is discussed in *SI Appendix*. Such sections also experience shrinkage during the preparation and during the electron microscopy (20). Our scaling for the dimensional changes is also discussed in *SI Appendix*.

Z-band subvolumes within the tomogram were extracted from the Z-band areas in the tomogram (*SI Appendix*, Fig. S1*D*) and averaged using the subtomogram averaging program PEET (21, 22). Semiautomated particle picking was performed by iterative refinement starting from a manually chosen single-particle initial reference and a uniform, 2D grid of initial locations with spacing approximating that of the unit cell. Selected points were windowed via cross-correlation thresholding and manual editing before further alignment and averaging, giving 483 points.

The basis for the subtomogram averaging was as follows: An actin filament is composed of a helix of actin monomers as shown schematically in Fig. 1*F* with colored spheres representing actin monomers. Adjacent red and blue spheres each with a short stub (referred to here as a symmetry pair) highlight symmetry-related points along the filament which are relevant for Z-band assembly. We assumed symmetry for actin comprising 28 subunits in 13 turns of the short pitch helix (28/13, also called genetic helix) as found previously in insect flight muscle (23), nemaline rod (24), and skeletal muscle Z-bands (25), which connects every actin subunit, giving a 167.1° rotation per subunit. Combined with an axial rise per subunit of 27.4 Å (23), after 7 subunits we have net rotation of 90° i.e., a 1/4 turn, and an axial displacement of 192 Å. The full axial repeat of the system comprises 28 subunits spanning 768 Å. A special feature of a symmetry pair is that the 2 links on either side of a filament have a relative 27.4-Å offset, giving a distinct asymmetric appearance. While visible in our subtomogram averages, this offset is a weak feature at the resolution achieved. In addition the 167.1° rotation is close to 180°, which tends to give the illusion of 2-fold rotational symmetry. Subtomogram averaging was applied at the subvolume coordinate as well as ±192-Å translation along the filament accompanied respectively with ±90° rotation. Two C2 axes orthogonal to the filament axis were identified with relative axial shifts of ±192 Å (shown by arrow in Fig. 2*A*). Starting from the 483 particles, these symmetry operations provided 5,796 asymmetric units for subtomogram averaging. Additional symmetries are expected and present, but their use for subtomogram averaging was precluded by the chosen subvolume size and the limited $z$ height included in the tomogram, e.g., see *SI Appendix*, Fig. S3*B*. The resolution of the average was estimated by a Fourier shell correlation (FSC) plot (*SI Appendix*, Fig. S2) which gave a value of 39 Å for a cutoff of 0.5. This is a good value for a plastic-embedded sample. Note that despite the FSC giving a value that would predict the visibility of actin subunits, no actin subunits are resolved in either the raw tomograms or the subtomogram averages. This could mean that the actin filaments are insufficiently preserved to retain visibility of the actin subunits in the tissue blocks or the sections, or it may be due to the unfavorable orientation of the filaments for viewing the F-actin subunits in the transverse sections.

The Z-band average was computationally cloned back into the original tomogram; 3 projection images are shown in *SI Appendix*, Fig. S3 and a walk through of the stack is shown in Movie S2. The cross-sectional image (*SI Appendix*, Fig. S3*A*) replicates features of the raw tomogram projection (*SI Appendix*, Fig. S1*D*) in a noise reduced form. *SI Appendix*, Fig. S3 *B* and *C* shows thin and thick, edge-on projections along the black line in *SI Appendix*, Fig. S3*A*. *SI Appendix*, Fig. S3*B* shows that there are about 3 half-repeats of 384 Å in the depth of the tomogram, while Fig. S3*C* shows a typical chevron appearance of the Z-band comparable with a regular electron microscope image of the basketweave Z-bands in sonic muscle (Fig. 1*B*).

**The 3D Structure of the Z-Band and Docking of Actin and α-Actinin.** We describe the results of the subtomogram averaging of the basketweave Z-band in Fig. 2, *SI Appendix*, Fig. S4, and Movie S3. Fig. 2 is composed of 3 columns (1–3). The region displayed comprises about 1 unit cell in cross-section with 2 actins of one orientation and 2 of the opposite orientation. The axes are shown in all of the panels, color coded red, green, and blue for $x$, $y$, and $z$ axes, respectively. Column 1 shows surface rendered views of the subtomogram average, *A* as a transverse view and *D*, *G*, *J* as longitudinal views showing *D* [11] view, *G* [10] view, and *J* [01] view. The transverse view in Fig. 2*A* shows very clear basketweave motif. In the longitudinal views the striking features of the reconstruction are vertical posts with arrowheads, the actin filaments cross-linked with great regularity by diagonal struts that are α-actinin. The links are slab-like with a flattened cross-section; the narrow side is observed in the transverse view (*A*) and the wider side is seen in the longitudinal [11] view in *D*. The actin filaments appear smooth at the resolution of the current analysis and individual monomers are not readily apparent.

For the fitting of actin and α-actinin into the 3D map (Fig. 2, column 2), we have used the 16-Å cryo-EM reconstruction of actin filament labeled with the ABD of α-actinin (PDB ID code 3LUE) (26). We first constructed an atomic model of actin with 28/13 symmetry based on the Holmes actin filament model (27). Then using Pymol (http://www.pymol.org) we added to this model the α-actinin ABD of Galkin et al. (26) at the Z-band relevant symmetry positions (Fig. 1*F*). The actin-ABD composite can be seen more clearly in the right column of Fig. 2 with the ABD shown in red. For α-actinin fitting, we first isolated the rod domain by deleting the ABD and EF hands at residues 247 and 784 for both monomers of α-actinin. Column 2 of Fig. 2 shows the result of fitting into a semitransparent version of the map, the actin-ABD and α-actinin rod. Actin filament coordinates of one orientation are colored green and the opposite orientation colored yellow; the arrows on the actins in Fig. 2 *J* and *L* point toward the M-band. The ABD, colored red, is the dominant feature of the actin filaments in the map. The actin-ABD composite greatly helped in docking into the map. The transverse view (*B*) is dominated by the curved Z-band links into which the curved rods fit nicely. As shown in Fig. 1 *G* and *H*, the rod atomic structure comprises a slab-like profile, which docks nicely into the slab-like profile of the links. In the longitudinal views, for clarity, only 2 pairs of rods colored blue and purple are docked into the map. The fit of these features is excellent at this resolution.

In column 3 of Fig. 2 we examine the atomic coordinates in the absence of the map to see the underlying structure. The transverse view (*C*) clearly shows the origin of the basketweave motif. The ABDs along each actin filament line up in projection showing 4 prominent densities (red). In the square formed by the

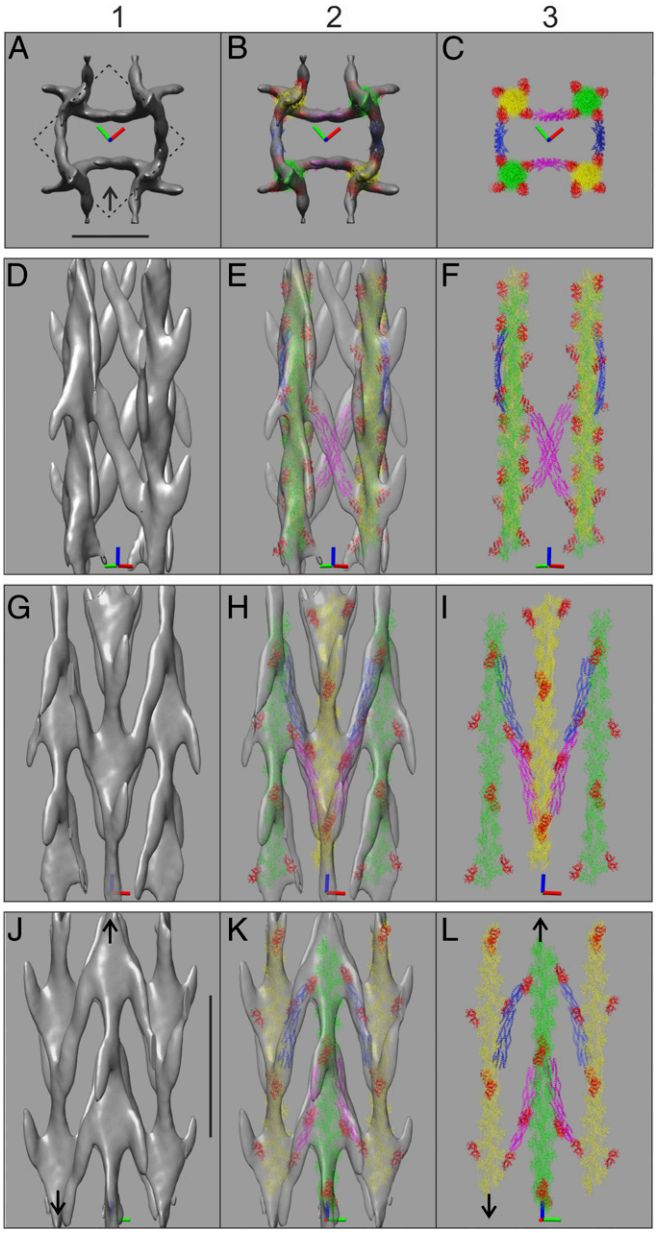


**Fig. 2.** Subtomogram average of the sonic muscle basketweave Z-band and fitting of atomic coordinates. Three columns are shown: Column 1, surface rendered views of subtomogram average; column 2, docked atomic coordinates of actin and α-actinin; and column 3, only the atomic coordinates. Color-coded axes are shown: *x*, red; *y*, green; and *z*, blue. The 1st row (*A*–*C*) shows transverse view; the 2nd row (*D*–*F*) shows longitudinal [11] view; the 3rd row (*G*–*I*) shows [10] view; and the 4th row (*J*–*L*) [01] view. The arrows on the actin filaments (*J* and *L*) point toward the M-band; in the opposite direction is the actin barbed end (which resides in the Z-band). Column 1 shows the clearest reconstruction of vertebrate muscle Z-band to date. It shows a unit cell of the Z-band (dashed box in *A*) composed of 2 pairs of actin filaments with opposite orientation and a pair of α-actinins linking 2 antiparallel actins at a given axial level. Pairs of links separated axially by 1/4 repeat (192 Å) are perpendicular to each other, yielding links to each actin filament in a rectangular motif (*A*). Column 2 shows the map with docked actins, 2 in yellow of one orientation, and 2 in green of the opposite orientation. Added to actin coordinates are selected actin binding domains of α-actinin depicted in red. For clarity, only 2 pairs of α-actinin rods are shown, in purple and blue. In transverse view (*B*) the arc of the rod matches nicely the gentle curve of the map link. Column 3 showing only the atomic coordinates demonstrates that the actin/α-actinin assembly in the Z-band is sensible. The chevron motif (*G*) typical of longitudinal views is due to projection of multiple actins in the depth and is composed of 2 axially consecutive layers of α-actinin (purple and blue in *I*) giving an apparent repeat of 384 Å. This figure was prepared using Chimera (41). Scale is indicated in *A* for the transverse views by [11] lattice spacing of 185 Å and in *J* for longitudinal views by a vertical bar depicting 384 Å (half-actin repeat).

4 actin filaments, 2 of one polarity (e.g., yellow) and 2 of the opposite (green), the ABDs are located either closer to the center of the square and linked by purple rods, or further out and linked by blue rods. This near rectangular shape with inward and outward curved edges gives rise to the basketweave motif. We note that α-actinin links actins in the [11] plane at an angle of 25° from the actin axis. The [11] view (Fig. 2*F*) shows why the [11] view in the electron micrographs comprises dense bands (Fig. 1*C*) in contrast to the [10] view (Fig. 1*B*). The dense bands arise from the ABDs and some rods (blue) lining up the sides of the actin filaments. The [10] view (Fig. 2*I*) shows the origin of the chevron motif. The motif arises due to the projection of 2 sets of linking rods at different but adjacent levels, e.g., blue and purple, giving an apparent periodicity of 384 Å. This effect is not apparent in the [01] view (Fig. 2*L*) as the relevant linking rods have not been drawn.

**Modeling the Mechanics of the Z-Band.** From the results of this study, we can start to investigate how tension generated in each sarcomere during contraction is handled in the Z-band. We constructed a simple model comprising 2 sets of actin filaments from adjoining sarcomeres on an interdigitating 262 Å square lattice extending over a circular area about 0.5 μm in diameter (*SI Appendix*, Fig. S5 *A* and *B* shows a longitudinal and a transverse section, respectively). α-Actinin was represented by thin cylinders of length 360 Å (full length of α-actinin including the ABD) connecting the actin filaments at the ABD attachment positions. The antiparallel actins were linked with 4 layers of α-actinin, each adjacent layer being separated by 192 Å and with a relative rotation of 90°. The actins along the circumference of the model were immobilized to simulate the sarcolemma and extracellular matrix; however, the spatial extent of the model is such that the effect of the sarcolemma is not felt in the central region of the model. The attachment point of α-actinins to actin and the ends of actin are considered nodes (represented by red spheres) and the portions of actin filaments between nodes and the α-actinins are considered segments. All segments were modeled as Hookean springs with an elastic constant of 2,280 pN/Å. No rotational constraints were applied to the segments at the nodes and all interconnected segments are linked via a node. Initially none of the nodes were subject to external forces and all segments measured zero tension. Since during an isometric contraction of a vertebrate striated muscle the tension per myosin filament in a half sarcomere rises to an estimated 480 pN (28), we assume here that such tension translates to 240 pN per actin filament in the half sarcomere's I-band. For our first simulation, we applied a force to each outer node of the actin filaments. These forces were directed upwards for the nodes at the *Top* of the model, and downward for the nodes at the bottom (*SI Appendix*, Fig. S5*E*). These forces had nominal value of 100 (corresponding to 100% of 240 pN) (*SI Appendix*, Fig. S5 *C*–*E*). The levels of tension calculated for the actin and α-actinin segments are shown in *E*. While the actin filaments on both sides have tension of 100, the tension in the α-actinins is progressively less toward the center of the Z-band (*E*) from 21 to 8. The lateral component of the tension is transmitted to the boundary of the whole region. To clarify what is done below, it is worth pointing out that the modeled region represented here corresponds to the central region of the constructed model and that the tension values would be the same if the actin outer nodes at the bottom of the model were anchored, i.e., kept fixed in space instead of having a force applied on them.

We next investigated the question of what the effect of an actin filament having a different tension is to its neighbors as could happen in a muscle during contraction. This is illustrated

in the diagram of *SI Appendix*, Fig. S5*F*, corresponding to the central region of the full 3D model shown in *SI Appendix*, Fig. S5 *A* and *B*. In this model the force applied to one of the actin outer nodes (marked with * in the diagram) is 10% bigger than the forces applied to all of the other actin outer nodes. Also, the actin outer nodes at the bottom of the model are anchored (this allows us to measure the changes in tension of the actin filaments, which would not be possible if a force was applied to the outer nodes and they were allowed to move). We found the 10% extra tension to be equally subdivided among the immediate neighboring actins of the opposite side and very little beyond (compare the tension values in *SI Appendix*, Fig. S5 *E* and *F*). This simulation demonstrates the remarkable efficiency and small spatial extent of the shock absorber nature of the Z-band in smoothing out the variations that must occur in the tension produced by the myriads of myosin cross-bridges acting on the actin filaments.

## Discussion

While great progress has been made in understanding the molecular structures of the actin, myosin, and their interaction in various states, little is known about the molecular structure of the sarcomeric skeleton like the Z-band and M-band. Understanding the molecular structure of the Z-band is important to understand how the tension generated during contraction is relayed by the Z-band from sarcomere to sarcomere along the myofibril. We have presented here the detailed structure of the Z-band in vertebrate striated muscle, giving details of the conformation and interaction of actin and α-actinin. We have found that the Z-band cross-link is composed of α-actinin linking actin filaments mainly in the [11] plane and has an angle of 25° off the actin filament. The whole α-actinin link is quite straight with the ABD roughly following the path of the rod. Two important features of the rod have a distinct fit into the map. The slightly curved rod exactly matches the curvature of the link. Secondly the flattened slab-like profile of the rod matches the similar profile of the link in the map, giving edge-on views of the slab in transverse view and face view for the diagonal link in the [11] longitudinal view.

**Comparison with Previous Z-Band 3D Studies.** Two previous 3D reconstructions of basketweave Z-bands have been reported (5, 29). Luther (29) investigated the structure of the Z-band in fish fin muscle, a fast muscle with a Z-band of width ∼700 Å, and by modeling, inferred that the number of α-actinin layers comprising it was 3. Luther et al. (5) studied bovine neck muscle, a slow muscle with a Z-band width of ∼1,300 Å and also by modeling, inferred that the number of layers was 6. Because of the low resolution of the reconstructions, ∼100 Å, no attempt was made to dock atomic models. The reconstructions look similar to the sonic Z-band obtained here.

Two small-square Z-band reconstructions have been reported. Morris et al. (24) investigated the Z-band in nemaline rods found in skeletal muscle of humans with nemaline myopathy. Like the sonic muscle Z-band, nemaline rods comprise extended Z-band assemblies but in the small-square form. The reconstruction showed that the small-square Z-band did not have curved links but comprised links with right angle bends. Morris et al. (24) proposed that the 4 actin filaments within each unit cell shown in Fig. 1*E* were linked by 2 α-actinins with the rods located in the middle in close proximity and running parallel to the actin filaments. Burgoyne et al. (30) studied the Z-band in rat cardiac muscle using dual-axis tomography and subtomogram averaging. In both cases the resolution was not sufficient for atomic docking.

**Suitability of Sonic Muscle to Study Z-Band Structure.** The sonic muscle Z-band is special because it is extraordinarily ∼1.2 μm wide in comparison with normal Z-bands which range from 70 to 150 nm. It exhibits the basketweave form homogeneously over the whole muscle. In comparison, normal muscle myofibrils show the basketweave form or the small-square lattice form, but often both may be present in a single myofibril in various proportions (2). The sonic muscle Z-band is highly crystalline, hence it is ideal for structural analysis as it provides many easily identifiable subvolumes for input into subtomogram averaging.

The Z-band structure reported here pertains to the interior of the Z-band. Lacking in our analysis is structural information on the axially outermost links on each side of the Z-band (facing outward to the M-bands). Hence the Z-band structure reported here would be expected between, for example, link levels 2 and 5 in a 6-layer Z-band as found in slow and cardiac muscle (1). The axially outermost α-actinin link is predicted to be different as it may interact with titin (31). We note that while normal Z-bands have precisely defined widths (1, 5, 6, 29) with precisely defined edges, the outer edges of the sonic muscle Z-band appear quite ragged (Fig. 1*A*), hence would not be suitable for determining outer-edge link structure.

An important difference between sonic muscle Z-band and normal Z-bands may be in the presence of titin. Titin, the third most abundant protein in muscle, is ∼1 μm long and spans half sarcomeres from the M-band to the Z-band (32, 33). It is responsible for maintaining the passive elasticity of muscle, hence its tethering mechanism at both ends is important. The part of titin present in the Z-band is composed of 2 to 7 45-residue Z-repeats, the number varying with the muscle isoform (31, 34). We do not know the form of titin present in the sonic muscle Z-band, whether it spans the full width of the Z-band or in fact whether it is present in the first place. In normal Z-bands, the Z-repeats of titin are thought to bind to EF3-4 hands of α-actinin under the action of phospholipids which induce the open state of the ABD (11, 35, 36). At the current resolution it is difficult to distinguish between the open and closed conformations of ABD, so we cannot draw any effective conclusions on the ABD conformation. Therefore, for our modeling we have used the conformation of CH1 domain of ABD due to the availability of its structure bound to actin by Galkin et al. (26). The anticipated flexibility in the linkage between the ABD and the α-actinin rod would mean that the angle of the α-actinin rod is quite closely constrained by the density in the map so this is not likely to be significantly affected by the choice of ABD conformation. A future high-resolution tomography study of a normal Z-band will be required to unravel the 3-dimensional structure of actin-ABD binding as well as binding of α-actinin EF3-4 to titin Z-repeats. Previous studies have suggested that titin may span the width of normal Z-bands (37, 38). A recent study using optical tweezers by Grison et al. (35) has shown that the few, 2 to 7, Z-repeats of titin interacting with EF3-4 hands of the consecutive α-actinin layers in the Z-band may be sufficient to tether the titin N terminus at the Z-band. Although it is unlikely that titin spans the width of the superwide sonic Z-band, we can assume from the Grison et al. (35) study that the presence of a few Z-repeats only at the outer edges of the sonic Z-bands would be sufficient to ensure mechanical stability of titin and the sarcomere.

**Comparison of Tomography of Sonic Muscle Z-Band Using Transverse and Longitudinal Sections.** For this study, the tomography analysis was done for both transverse (TS) and longitudinal (LS) sections. In each case, dual-axis tomography was done followed by subtomogram averaging. The reconstruction from LS was not as informative as the TS, so it has not been described here. The reduced effectiveness of the LS tomogram is due to the differential shrinkage during exposure to the electron beam (20). Shrinkage is most pronounced along the tomogram *z* axis, and is often corrected by applying an appropriate stretch. For the LS tomogram, α-actinin links with different orientations will undergo differential shrinkage, and the results will be merged together during subtomogram averaging resulting in blurring and loss of resolution, which cannot be corrected by stretching. For the TS studies here, the dual-axis tomogram revealed excellent detail into which molecular docking could be done. Since the TS and LS averages are not equivalent, combining the 2 datasets was not pursued.

**Mechanical Aspects of the Z-Band.** In this study we have established the geometry of the basketweave Z-band; hence, we can investigate how tension is handled in the Z-band. Our simple model to investigate the tensions in actin and α-actinin during contraction (*SI Appendix*, Fig. S5) demonstrated the shock-absorbing nature of the Z-band in smoothing out the variations that must occur in the tension produced by the myriads of myosin cross-bridges acting on the actin filaments. We would expect the shock-absorbing effect to be much greater in slow and cardiac muscles with up to 6 layers of α-actinin compared with the narrow Z-bands in fast-twitch muscles with 2 layers. The contractile tension in the Z-band also has a transverse component. In striated muscle, desmin intermediate filaments connect neighboring myofibrils at the level of the Z-band. Mutations or deficit in desmin lead to skeletal or cardiac muscle disease (39) showing the importance of the transverse cytoskeletal network which the Z-band is part of.

## Materials and Methods

**Muscle Preparation.** Full details of the muscle preparation are given in *SI Appendix*. Briefly, fibers of swimbladder muscle (sonic muscle) of midshipman fish were rapidly frozen, freeze substituted, embedded in resin, ∼100-nm thin transverse sections cut, coated with 10-nm gold fiducials, and stained with uranyl acetate and lead citrate.

**Electron Microscopy.** Dual-axes tilt series were recorded with an FEI CM200 electron microscope using a Gatan 916 high tilt holder over the 2 ranges −62° to 70° and −70° to 70° in steps of 2°. The tilt series images were recorded using the automated procedure provided by Tietz EM-Menu software. The images were recorded at 27,000× magnification on a Tietz FC415 camera with 4 k × 4 k pixel resolution (https://www.tvips.com). The images were binned 2× and the final pixel size was 6.42 Å. Tomography and combination of dual-axes tilt series were done using IMOD (40). The software PEET running under ETOMO was used for subtomogram averaging (21, 22). The Z-band subvolume marked by the dashed outline box (Fig. 1*E*) was defined as the "particle" for subtomogram averaging. Automatic particle picking was performed by iterative refinement starting from a manually chosen initial reference and a uniform 2D grid of initial locations with spacing approximating that of the unit cell. Selected points were windowed via cross-correlation thresholding and manual editing before further alignment and averaging.

**ACKNOWLEDGMENTS.** We thank Hanspeter Winkler for help with the longitudinal section tomography and subtomogram averaging, Andrey Tsaturyan and William Lehman for helpful discussions, and John Wright of University of Texas at Austin for technical assistance. P.K.L. was supported by British Heart Foundation Programme Grant RG/11/21/29335. K.A.T. and J.L. were supported by NIH Grant GM30598. K.W. was supported by the Intramural Research Program of NIAMS and by Taipei Medical University, Taiwan. Molecular graphics and analyses were performed with University of California San Francisco (UCSF) Chimera program, developed by the Resource for Biocomputing, Visualization, and Informatics at UCSF, with support from NIH P41-GM103311.

1. P. K. Luther, The vertebrate muscle Z-disc: Sarcomere anchor for structure and signalling. *J. Muscle Res. Cell Motil.* **30**, 171–185 (2009).
2. R. J. Perz-Edwards, M. K. Reedy, Electron microscopy and x-ray diffraction evidence for two Z-band structural states. *Biophys. J.* **101**, 709–717 (2011).
3. M. A. Goldstein, L. H. Michael, J. P. Schroeter, R. L. Sass, Structural states in the Z band of skeletal muscle correlate with states of active and passive tension. *J. Gen. Physiol.* **92**, 113–119 (1988).
4. P. K. Luther, Symmetry of a vertebrate muscle basketweave Z-Band. *J. Struct. Biol.* **115**, 275–282 (1995).
5. P. K. Luther, J. S. Barry, J. M. Squire, The three-dimensional structure of a vertebrate wide (slow muscle) Z-band: Lessons on Z-band assembly. *J. Mol. Biol.* **315**, 9–20 (2002).
6. P. K. Luther, R. Padrón, S. Ritter, R. Craig, J. M. Squire, Heterogeneity of Z-band structure within a single muscle sarcomere: Implications for sarcomere assembly. *J. Mol. Biol.* **332**, 161–169 (2003).
7. D. Frank, C. Kuhn, H. A. Katus, N. Frey, The sarcomeric Z-disc: A nodal point in signalling and disease. *J. Mol. Med. (Berl.)* **84**, 446–468 (2006).
8. C. A. Otey, O. Carpen, Alpha-actinin revisited: A fresh look at an old player. *Cell Motil. Cytoskeleton* **58**, 104–111 (2004).
9. B. Sjöblom, A. Salmazo, K. Djinović-Carugo, Alpha-actinin structure and regulation. *Cell. Mol. Life Sci.* **65**, 2688–2701 (2008).
10. A. Blanchard, V. Ohanian, D. Critchley, The structure and function of alpha-actinin. *J. Muscle Res. Cell Motil.* **10**, 280–289 (1989).
11. Ede. A. Ribeiro, Jr *et al*., The structure and regulation of human muscle α-actinin. *Cell* **159**, 1447–1460 (2014).
12. C. M. Hampton, D. W. Taylor, K. A. Taylor, Novel structures for alpha-actinin:F-actin interactions and their implications for actin-membrane attachment and tension sensing in the cytoskeleton. *J. Mol. Biol.* **368**, 92–104 (2007).
13. J. Ylänne, K. Scheffzek, P. Young, M. Saraste, Crystal structure of the alpha-actinin rod reveals an extensive torsional twist. *Structure* **9**, 597–604 (2001).
14. P. K. Luther *et al*., Understanding the organisation and role of myosin binding protein C in normal striated muscle by comparison with MyBP-C knockout cardiac muscle. *J. Mol. Biol.* **384**, 60–72 (2008).
15. M. K. Lewis *et al*., Concentric intermediate filament lattice links to specialized Z-band junctional complexes in sonic muscle fibers of the type I male midshipman fish. *J. Struct. Biol.* **143**, 56–71 (2003).
16. A. H. Bass, M. A. Marchaterre, Sound-generating (sonic) motor system in a teleost fish (Porichthys notatus): Sexual polymorphism in the ultrastructure of myofibrils. *J. Comp. Neurol.* **286**, 141–153 (1989).
17. E. M. Ostap, 2,3-butanedione monoxime (BDM) as a myosin inhibitor. *J. Muscle Res. Cell Motil.* **23**, 305–308 (2002).
18. L. A. Amos, R. Henderson, P. N. Unwin, Three-dimensional structure determination by electron microscopy of two-dimensional crystals. *Prog. Biophys. Mol. Biol.* **39**, 183–231 (1982).
19. P. K. Luther, R. A. Crowther, Three-dimensional reconstruction from tilted sections of fish muscle M-band. *Nature* **307**, 566–568 (1984).
20. P. K. Luther, "Sample shrinkage and radiation damage of plastic sections" in *Electron Tomography: Methods for Three-Dimensional Visualization of Structure in the Cell*, J. Frank, Ed. (Springer, 2006), pp. 17–40.
21. J. M. Heumann, A. Hoenger, D. N. Mastronarde, Clustering and variance maps for cryo-electron tomography using wedge-masked differences. *J. Struct. Biol.* **175**, 288–299 (2011).
22. D. Nicastro *et al*., The molecular architecture of axonemes revealed by cryoelectron tomography. *Science* **313**, 944–948 (2006).
23. A. Miller, R. T. Tregear, Structure of insect fibrillar flight muscle in the presence and absence of ATP. *J. Mol. Biol.* **70**, 85–104 (1972).
24. E. P. Morris, G. Nneji, J. M. Squire, The three-dimensional structure of the nemaline rod Z-band. *J. Cell Biol.* **111**, 2961–2978 (1990).
25. P. K. Luther, J. M. Squire, Muscle Z-band ultrastructure: Titin Z-repeats and Z-band periodicities do not match. *J. Mol. Biol.* **319**, 1157–1164 (2002).
26. V. E. Galkin, A. Orlova, A. Salmazo, K. Djinovic-Carugo, E. H. Egelman, Opening of tandem calponin homology domains regulates their affinity for F-actin. *Nat. Struct. Mol. Biol.* **17**, 614–616 (2010).
27. K. C. Holmes, D. Popp, W. Gebhard, W. Kabsch, Atomic model of the actin filament. *Nature* **347**, 44–49 (1990).
28. G. Piazzesi *et al*., Skeletal muscle performance determined by modulation of number of myosin motors rather than motor force or stroke size. *Cell* **131**, 784–795 (2007).
29. P. K. Luther, Three-dimensional structure of a vertebrate muscle Z-band: Implications for titin and alpha-actinin binding. *J. Struct. Biol.* **129**, 1–16 (2000).
30. T. Burgoyne, E. P. Morris, P. K. Luther, Three-dimensional structure of vertebrate muscle Z-band: The small-square lattice Z-band in rat cardiac muscle. *J. Mol. Biol.* **427**, 3527–3537 (2015).
31. P. Young, C. Ferguson, S. Bañuelos, M. Gautel, Molecular structure of the sarcomeric Z-disk: Two types of titin interactions lead to an asymmetrical sorting of alpha-actinin. *EMBO J.* **17**, 1614–1624 (1998).
32. H. Granzier, S. Labeit, Structure-function relations of the giant elastic protein titin in striated and smooth muscle cells. *Muscle Nerve* **36**, 740–755 (2007).
33. K. Wang, J. McClure, A. Tu, Titin: Major myofibrillar components of striated muscle. *Proc. Natl. Acad. Sci. U.S.A.* **76**, 3698–3702 (1979).
34. M. Gautel, D. Goulding, B. Bullard, K. Weber, D. O. Fürst, The central Z-disk region of titin is assembled from a novel repeat in variable copy numbers. *J. Cell Sci.* **109**, 2747–2754 (1996).
35. M. Grison, U. Merkel, J. Kostan, K. Djinović-Carugo, M. Rief, α-actinin/titin interaction: A dynamic and mechanically stable cluster of bonds in the muscle Z-disk. *Proc. Natl. Acad. Sci. U.S.A.* **114**, 1015–1020 (2017).
36. P. Young, M. Gautel, The interaction of titin and alpha-actinin is controlled by a phospholipid-regulated intramolecular pseudoligand mechanism. *EMBO J.* **19**, 6331–6340 (2000).
37. C. Knupp, P. K. Luther, J. M. Squire, Titin organisation and the 3D architecture of the vertebrate-striated muscle I-band. *J. Mol. Biol.* **322**, 731–739 (2002).
38. A. D. Liversage, D. Holmes, P. J. Knight, L. Tskhovrebova, J. Trinick, Titin and the sarcomere symmetry paradox. *J. Mol. Biol.* **305**, 401–409 (2001).
39. Y. Capetanaki, S. Papathanasiou, A. Diokmetzidou, G. Vatsellas, M. Tsikitis, Desmin related disease: A matter of cell survival failure. *Curr. Opin. Cell Biol.* **32**, 113–120 (2015).
40. J. R. Kremer, D. N. Mastronarde, J. R. McIntosh, Computer visualization of three-dimensional image data using IMOD. *J. Struct. Biol.* **116**, 71–76 (1996).
41. E. F. Pettersen *et al*., UCSF Chimera–A visualization system for exploratory research and analysis. *J. Comput. Chem.* **25**, 1605–1612 (2004).